CrystEngComm

Accepted Manuscript

ROYAL SOCIETY OF CHEMISTRY

www.rsc.org/crystengcomm

[JOURNAL NAME HERE] | www.rsc.org/[JOURNAL] Paper

Synthesis of one-dimensional WO_3-Bi_2WO_6 heterojunctions with enhanced photocatalytic activity

Yin Peng*[a], Qing-Guo Chen[a], Dan Wang[a], Hai-Yan Zhou[a] and An-Wu Xu*[b]

Receipt/Acceptance Data **[DO NOT ALTER/DELETE THIS TEXT]**
Publication data **[DO NOT ALTER/DELETE THIS TEXT]**
DOI: 10.1039/b000000x [DO NOT ALTER/DELETE THIS TEXT]

WO_3-Bi_2WO_6 heterostructures were synthesized by a facile hydrothermal method using WO_3 nanorods and $Bi(NO_3)_3$ solution as raw materials. The Bi_2WO_6 nanosheets uniformly anchored on the surface of WO_3 nanorods. The photocatalytic activity of the samples was assessed for degradation of Rhodamin B (RhB) and phenol under solar light irradiation. The WO_3-Bi_2WO_6 heterostructures showed higher photocatalytic activities than pure WO_3 and Bi_2WO_6. As the content of Bi_2WO_6 increases, the photocatalytic activity of WO_3-Bi_2WO_6 heterojunction enhanced and the optimal sample was WO_3-Bi_2WO_6 with the mole ratio nWO_3:nBi^{3+} of 5:3. The efficient separation of electron-hole pairs because of the stagger band potentials between WO_3 and Bi_2WO_6 may account for the higher photoactivity of WO_3-Bi_2WO_6 hybrid structures. Radical scavenger experiments indicate that holes (h^+) and superoxide radicals ($\bullet O_2^-$) were the main active species for RhB degradation during photocatalytic process.

Introduction

As a green technology for practical applications in new energy conversion and environmental purification, semiconductor photocatalysis has drawn ever-increasing worldwide interest. However, the rapid recombination of photogenerated charge carriers for single semiconductor has seriously inhibited photocatalytic performance. The way to coupling two kinds of photocatalysts to form heterojunction offers the chance to design a new photocatalyst with high photocatalytic activity. This way has some advantages: (1) effective charge separation can be achieved; (2) high reduction power and deep oxidation power can be simultaneously obtained even by using visible light; and (3) various photocatalysts can be paired.[1-6] Some researches[7-11] have proved that heterojunction photocatalysts can efectively improve the seperation of photogenerated electron-hole pairs and expand the photo-absorption range.

As an important n-type visible-light photocatalyst with narrow band gap (2.4–2.8 eV), WO_3 has attracted considerable attention due to some excellent properties. For instance, stable physicochemical properties,[12-15] resilience to photocorrosion effect in aqueous solution[16-19] and good electron transport properties.[20] So, nanostructured WO_3 is generally considered as a feasible candidate for visible-light photocatalysts. However, pure WO_3 nanomaterials are usually not efficient photocatalysts, because of the high electron–hole recombination rate. Thus, some WO_3 heterojunctions have been designed to improve its photocatalytic activity.[21-28]

Bi_2WO_6 is one of the simplest Aurivillius oxides, which possesses a layered structure with the perovskite-like slab of WO_6, and has been utilized as excellent photocatalyst for degradation of organic compounds under visible light irradiation due to its good photocatalytic performance.[29–31] Bare Bi_2WO_6 can absorb UV light and visible light with wavelength less than ca. 450 nm, which overlaps a small part of the solar spectrum. However, the rapid recombination of photogenerated charge carriers largely limits the photoactivity of Bi_2WO_6 material. Bi_2WO_6 and WO_3 have suitable band to form a heterojunction photocatalyst, which can effectively improve the separation of photogenerated charge carriers. Herein, we design to synthesize one-dimensional (1D) WO_3-Bi_2WO_6 heterojunction via a facile hydrothermal method using WO_3 nanorods and $Bi(NO_3)_3$ solution as raw materials.

One-dimensional (1D) semiconductor has the potential to produce high photoactivity due to their fast charge transport properties and the expected reduced length scales for minority carrier diffusion in single crystalline nanostructures. In this article, one-dimensional WO_3-Bi_2WO_6 heterojunctions with high photocatalytic activity were prepared. Bi_2WO_6 nanosheets are uniformly *in situ* anchored onto the surface of WO_3 nanorods. This 1D heterostructure displays superior photocatalytic activity for degradation of the RhB under solar light irradiation. Radical scavenger experiments indicate that holes (h^+) and superoxide radicals ($\bullet O_2^-$) are the main active species for RhB degradation during photocatalytic process. The photocatalytic mechanism of WO_3-Bi_2WO_6 heterojunction is discussed according to the position of the valence band (VB) and conduction band (CB), combined with band gap (Eg) of WO_3 and Bi_2WO_6.

Experimental Section

Photocatalyst preparation

All the reagents used in our experiment were analytical grade and used as received without further purification.

WO_3 nanorods were synthesized according to report in ref 32. 0.825 g of $Na_2WO_4 \bullet 2H_2O$ and 0.580 g of NaCl were dissolved in 19 mL of deionized water. Subsequently, 3 M HCl was slowly dropped into the solution with stirring until the pH value of the solution reached 2.0. The solution was transferred into a Teflon-lined autoclave and heated at 180 ºC for 24 h. The obtained product was repeatedly washed with deionized water for 3 times.

[a]The Key Laboratory of Functional Molecular Solids, Ministry of Education, College of Chemistry and Materials Science, Anhui Normal University, Wuhu 241000, China
[b]Division of Nanomaterials and Chemistry, Hefei National Laboratory for Physical Sciences at Microscale, Department of Chemistry, University of Science and Technology of China, Hefei 230026, P. R China.
Fax: (+86) 551-6360 2346; E-mail: anwuxu@ustc.edu.cn.
† Electronic Supplementary Information (ESI) available: [details of any supplementary information available should be included here]. See http://dx.doi.org/10.1039/b000000x/

Then, Bi_2WO_6-WO_3 nanorods were synthesized via a solvothermal process. 0.25 mmol of WO_3 nanorods and different amounts of $Bi(NO_3)_3$•$5H_2O$ were added into the 10 ml of ethylene glycol (EG) solution under sonication for 10 min. 30 mL of ethanol was added into above mixture under magnetic stirring for 1 h. The mixture was sealed into a Teflon-lined stainless steel autoclave and treated at 160 ºC for 20 h. After being cooled down to room temperature, the products were collected and washed several times with deionized water and absolute ethanol and dried at 60 ºC for 4 h. The as-obtained samples with the molar ratios of n_{WO3} : n_{Bi}^{3+} = 5:1, 5:3 and 5:5, were labelled S1, S2 and S3, respectively. Bi_2WO_6 control sample was obtained using Na_2WO_4 instead of WO_3 nanorods in above reaction system.

Photocatalytic activity measurements

Photocatalytic activity of the prepared WO_3-Bi_2WO_6 samples was measured by decomposing RhB under solar/visible light irradiation. The light source was a 500 W Xe lamp (PLS-SXE500/500UV, Trusttech Co., Ltd. Beijing). In a typical experiment, the photocatalyst (100 mg) was added into 100 mL of RhB (or phenol) (10 mg/L) to produce a suspension for the degradation reaction at room temperature. Before the solar/visible light irradiation, the suspension was stirred in the dark for 30 min to ensure an adsorption/desorption equilibrium of RhB (or phenol) on the surface of the photocatalyst. Then, the suspension was illuminated by the Xe lamp combined with a UV cut-off filter ($\lambda \geq 400$ nm) under stirring. At given time intervals, about 4 mL suspensions were withdrawn, and centrifuged to remove the precipitate. The degradation reaction process was monitored by measuring the concentration of RhB (or phenol) as a function of irradiation time in the solution with UV-Vis absorption spectra. Additionally, the recycling experiments were performed for five recycles to test the durability. After each cycle, the photocatalyst was centrifuged and used directly for the next experiment.

The method of active species trapping experiments is the same as the photoactivity tests. *P*-benzoquinone (BQ) (0.001 mol/L), disodium ethylenediaminetetraacetate (EDTA-2Na) (0.01 mol/L) and t-butanol (0.01 mol/L) were added into RhB solution to trap the superoxide radicals ($•O_2^-$), hole (h^+) and hydroxyl radicals (•OH), respectively, followed by photocatalytic test.

Characterization

Field emission scanning electron microscopy (FE-SEM) images were recorded on a Hitachi S-4800 microscope. Transmission electron microscopic (TEM) images, high-resolution transmission electron microscopic (HRTEM) images and the selected area electron diffraction (SAED) patterns were performed on a JEOL-2010 microscope with an accelerating voltage of 200 kV, and energy-dispersive X-ray spectroscopy (EDS) analysis was performed. High angle annular dark field scanning TEM (HAADF STEM) images and energy dispersive spectrum (EDS) were taken using an ultra-high resolution field emission gun transmission electron microscope (JEM-ARM 200F, Japan). X-Ray powder diffraction (XRD) was carried out on a Rigaku (Japan) D/max -γA X-ray diffractometer with Cu-Kα radiation ($\lambda = 0.154178$ nm).

UV-vis diffuse-reflectance spectra were measured with a UV-2450 spectrophotometer in the wavelength range of 200-800 nm at room temperature. $BaSO_4$ was used as the reflectance standard material. The X-Ray photoelectron spectroscopy (XPS) was performed on a Perkin-Elmer RBD upgraded PHI-5000C ESCA system.

Results and discussion

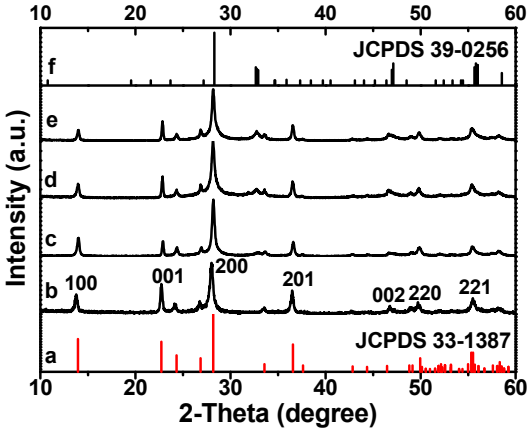

Fig. 1 The XRD patterns of (a, f) Standard Card of WO_3 and Bi_2WO_6, (b) WO_3 nanorods, (c) S1, (d) S2 and (e) S3.

X-ray powder diffraction (XRD) was used to identify the structure and phase composition. Fig. 1 shows the XRD patterns of WO_3-Bi_2WO_6 heterojunctions with different loaded-Bi_2WO_6 contents and pure WO_3 nanorods for comparison. All of the diffraction peaks in Fig. 1b can be well-indexed to the hexagonal structure of WO_3 (JCPDS No. 33-1387). The sharp and narrow diffraction peaks of WO_3 nanorods indicate the high degree of crystallinity. No traces of other impurity are detected, confirming the high purity of WO_3 sample. Fig. 1c–e obviously display two sets of XRD peaks of hexagonal WO_3 and orthorhombic Bi_2WO_6 (JCPDS No. 39-0256) with the absence of other impurity. Hence, WO_3-Bi_2WO_6 heterostructures are formed between WO_3 and Bi_2WO_6 components.

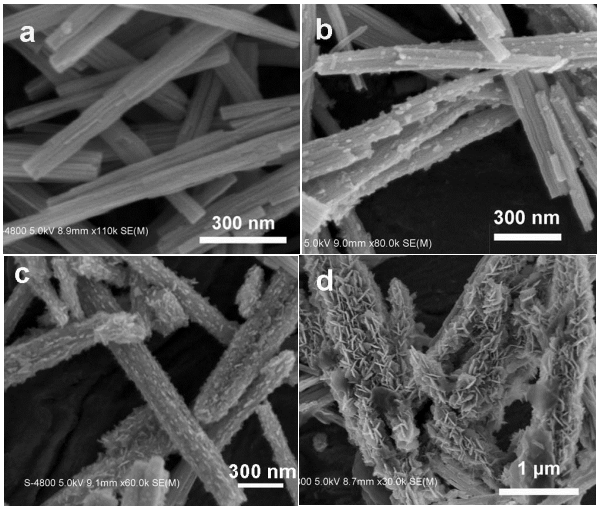

Fig. 2 FE-SEM images of (a) pure WO_3, (b) S1, (c) S2 and (d) S3.

Fig. 2 displays the SEM images of the WO_3-Bi_2WO_6 heterojunctions and WO_3 nanorods. From Fig. 2a, it can be clearly seen that the as-made WO_3 sample mainly consists of nanorods with the diameter of approximately 70–120 nm. The morphologies of WO_3-Bi_2WO_6 composites with different n_{WO3}: n_{Bi}^{3+} are shown in Fig. 2b-d. WO_3-Bi_2WO_6 heterojunctions still well maintain the rod-like structure. However, the surface of the WO_3 nanorods is no longer smooth. Instead, some secondary nanosheets decorate on the nanorods when the n_{WO3} : n_{Bi}^{3+} is 5:1 (Fig. 2b). With the concentration of Bi^{3+} ions increase, more and more Bi_2WO_6 nanosheets grow on the WO_3 nanorods (5:3, Fig.

2c). Furthermore, these nanosheets become slightly thick (S1→S2).When the $n_{WO3:}$ n_{Bi}^{3+} is 5:5 (S3), highly dense Bi_2WO_6 nanosheets were formed on the surface of the WO_3 nanorods (Fig. 2d). The SEM images with low magnification are provided in Fig. S1.

To further obtain information about the structure of the sample, the S2 heterojunction was characterized by transmission electron microscopy (TEM). As shown in Fig. 3a, it can be clearly seen the Bi_2WO_6 nanosheets grow onto the surface of the WO_3 nanorods, which is consistent with the SEM results. The energy dispersive spectroscopy (EDS) analysis (Fig. 3c) further confirms that these nanosheets only contain O, Bi and W elements (see red square inset Fig.3a), and the atomic ratio of Bi/W is calculated to be about 21.30 : 11.15, close to 2:1 ratio in Bi_2WO_6. Fig. 3b shows the high-resolution transmission electron microscopic (HRTEM) image of S2 taken from the edge of Bi_2WO_6 nanosheet (see red arrow in Fig. 3a). It is found that two sets of lattice fringes with interplanar spacing of 0.32 and 0.22 nm, which well corresponds to (131) and (132) planes of orthorhombic Bi_2WO_6, respectively.

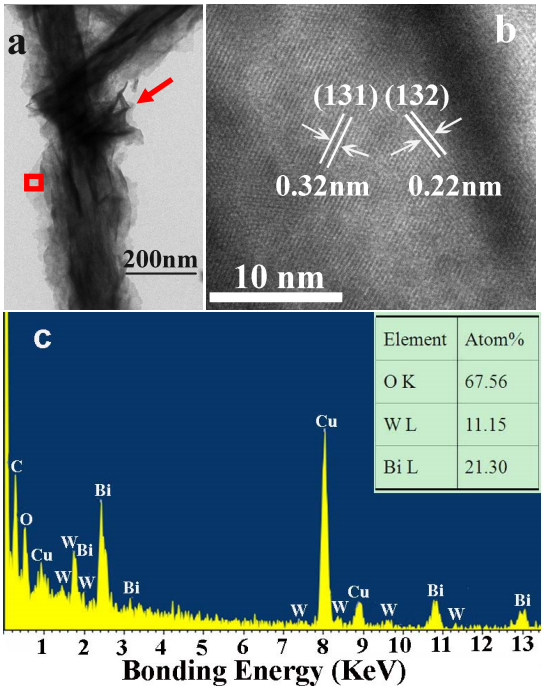

Fig. 3 (a) TEM, (b) HRTEM image and (c) EDS spectrum of the S2 heterojunction.

Further analysis using dark-field scanning TEM (STEM) (Fig. 4a) reveals contrast indicative of variations in the chemical composition as expected for the Bi_2WO_6-WO_3 heterostructure. Energy-dispersive X-ray spectroscopy (EDS) mapping of the same region (Fig. 4b-d) clearly defines the spatial distributions of Bi, W and O in an individual nanorod and illustrates that the W (Fig. 4c) element mainly distributes in the interior of Bi_2WO_6-WO_3 heterostructure while a small amount of W element spreads over the surface. According to the clear distribution of Bi and O elements (Fig. 4b, d), it is confirmed that Bi_2WO_6 nanoplates grow on the surface of WO_3 nanorods, which is consistent with XRD and TEM results.

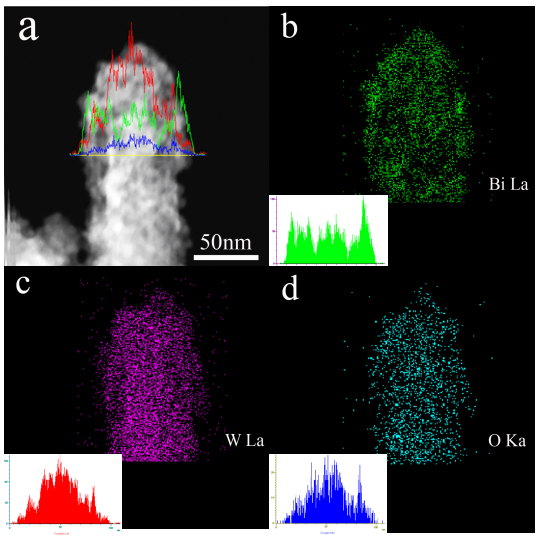

Fig. 4 STEM images of the S2 heterojunction (a) and the EDS element mapping of Bi (green) (b), W (pink) (c) and O (light blue) (d) ; the insets are the EDS line scanning of Bi ,W and O, respectively.

A possible formation mechanism for Bi_2WO_6-WO_3 heterojunctions might be proposed as shown in scheme 1. When WO_3 nanorods disperse into ethylene glycol solution under long time ultrasonic, the ethylene glycol molecules will adsorb on the surface of WO_3 nanorods. During heating process, WO_3 molecules on the surface react with hydroxyls from ethylene glycol and form WO_4^{2-} anions, which further react with Bi^{3+} and form Bi_2WO_6 nanoplates on the surface of WO_3 nanorods.

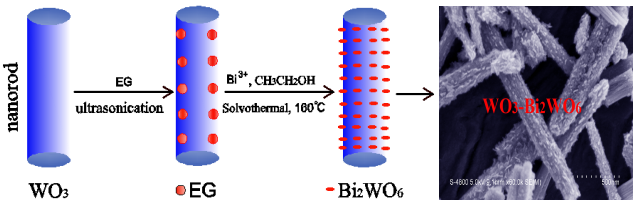

Scheme 1 Schematic illustration of the formation of WO_3-Bi_2WO_6 heterostructures.

The composition and chemical state of S2 sample was investigated by X-ray photoelectron spectroscopy (XPS). Fig. 5 represents the typical full survey and high-resolution spectra for Bi 4f, W 4f and O 1s peaks for S2. In Fig. 5a, O, Bi and W peaks appear in S2 heterojunction. The binding energy located at 35.5 eV and 37.6 eV is ascribed to W $4f_{7/2}$ and W $4f_{5/2}$ bands, respectively. The splitting energy of the 4f doublet of W is 2.1 eV, indicating that the valence state of W is +6 (Fig. 5b).[33] The peaks located at 164.5 and 159.2 eV are attributed to Bi $4f_{5/2}$ and Bi $4f_{7/2}$, respectively (Fig. 5c), which proves all the Bi species in S2 sample are in the form of Bi^{3+}. The O1s peak is deconvoluted into three peaks at 529.9, 530.9 and 532.2 eV. The low binding energy peaks at 529.9 and 530.9 eV is ascribed to the lattice oxygen, which are related to the Bi-O and W-O chemical bonding in the Bi_2WO_6 and WO_3. The higher binding energy peak at 532.2 eV is attributed to the surface hydroxyl oxygen (Fig. 5d).

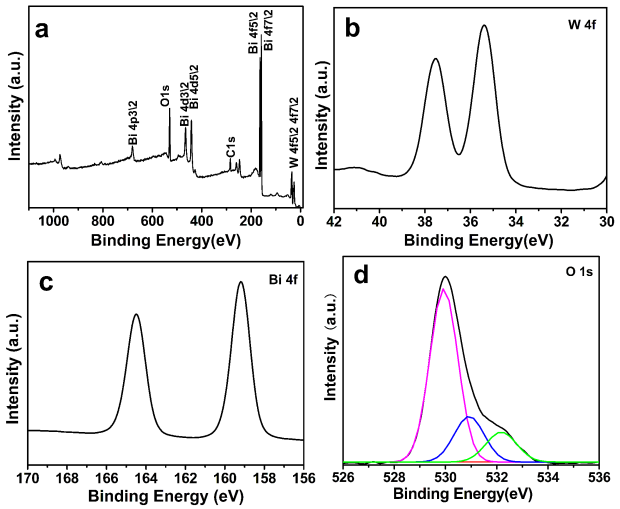

Fig. 5 (a) Survey XPS spectrum and high-resolution XPS spectra of (b) W 4f, (c) Bi 4f and (d) O 1s for S2 sample.

Adsorption and desorption experiments using N_2 were carried out at 77 K. Fig. 6a displays the nitrogen sorption isotherm of the S2 sample. The shape of the isotherm exhibits II-type isotherm with a type-H4 hysteresis loop at a high relative pressure (p/p_0) range of 0.45–1.0,[34,35] prominently indicating the presence of a macroporous structure in this material. This result can be further confirmed by the corresponding pore size distribution, as shown in Fig. 6b. Table S1 gives the BET surface area and pore volume of different samples. It can be found that the BET specific surface areas of the WO_3-Bi_2WO_6 structures are all lower than that of pure WO_3 nanorods (27 $m^2 \cdot g^{-1}$), but close to that of Bi_2WO_6 nanoflowers (15 $m^2 \cdot g^{-1}$). Therefore, the BET surface areas are not the main factor for affecting the photocatalytic activity of the obtained products. It also can be found from Table S1 that S2 sample has the largest pore volume among all the samples. As well-known, a suitable pore volume allows light waves to penetrate deep inside the photocatalysts and leads to high mobility of charge.[36-39] It is speculated that the largest pores in the S2 sample allow the penetration of light waves and phenol or RhB molecules in solution deep into the photocatalyst, which may greatly promote the photocatalytic activity.

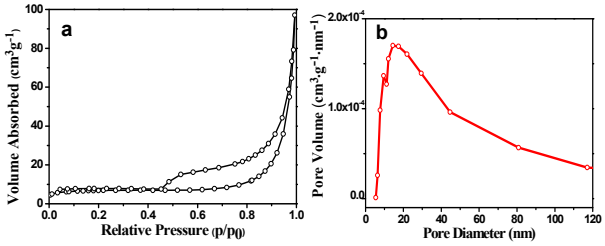

Fig. 6 (a) Nitrogen adsorption-desorption isotherm and (b) the corresponding pore size distribution of S2 sample.

The optical property of WO_3-Bi_2WO_6 heterojunctions (Fig. 7a) was measured by UV-vis diffuse-reflectance spectra (DRS), and their optical band gaps (Fig. 7b) can be determined by the following equation.[40]

$$\alpha h\nu = A(h\nu - Eg)^{n/2}$$

in which α, h, ν, A and Eg are the absorption coefficient, Planck constant, light frequency, a constant and band gap, respectively. And n equals to 1 for indirect band gap and 4 for direct band gap. here n = 1 for Bi_2WO_6[41] and n = 4 for WO_3.[42] In the Fig. 7b, the extrapolation of the $(\alpha h\nu)^{2/n}$ against hν plot on the x intercepts gives the optical band gap of 2.89 eV for Bi_2WO_6 and 2.81 eV for WO_3.

From Fig. 7a an interesting phenomenon can be found that the obtained WO_3 and S1, S2 and S3 samples possess strong near-infrared absorption property. More recently, obvious near-infrared light absorption of $W_{18}O_{49}$ nanomaterials caused by oxygen vacancies has attracted much attention.[43] Tian et al. also discovered that Bi_2WO_6 had good near-infrared photocatalytic degradation for methyl orange (MO).[44] Oxygen vacancies associated with tungsten ions in lower oxidation states (W^{5+}) than the 6+ expected in WO_3 stoichiometry may be the main reason for WO_3 with strong near-infrared absorption.[45] The oxygen vacancies in WO_3 can raise the Fermi level and reduce the band edge, allowing for interband transitions and carrier creation under near-infrared excitation.[44] With the content of Bi_2WO_6 increasing, the absorption intensity of near-infrared light becomes weak, which is due to the reaction loss of WO_3. The further research related to near-infrared absorption property of WO_3-Bi_2WO_6 heterojunction is underway.

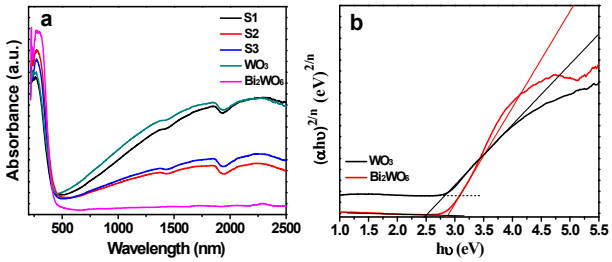

Fig. 7 (a) UV-Vis diffuse reflectance spectra of WO_3, Bi_2WO_6 and WO_3-Bi_2WO_6 samples, (b) the plots of $(\alpha h\nu)^{2/n}$ vs. hν (n = 4 for samples WO_3 and n = 1 for Bi_2WO_6).

The photocatalytic activity of the pure WO_3, Bi_2WO_6 and WO_3-Bi_2WO_6 heterojunctions were evaluated by degradation of RhB dye in aqueous solution under solar light irradiation. Fig. 8a depicts the correlation curves between the concentration changes of RhB solution and the irradiation time in the presence of photocatalysts. WO_3-Bi_2WO_6 samples exhibit higher photocatalytic activity than pure WO_3 and Bi_2WO_6. It is noted that the photocatalytic activity of WO_3-Bi_2WO_6 heterojunctions gradually increases with the loaded-Bi_2WO_6 content increasing (S2) and then decreases with further increasing Bi_2WO_6 content (S3). Therefore, S2 sample exhibits the best photocatalytic performance to degrade the RhB among all the photocatalysts. It can decompose 90% of RhB solution in 20 min under solar light irradiation. Obviously, the photocatalytic activity of the samples is significantly affected by the Bi_2WO_6 content in WO_3-Bi_2WO_6 composites. According to the SEM images (Fig. 2) of WO_3-Bi_2WO_6 heterojunctions, when the concentration of Bi^{3+} is low, only sparse Bi_2WO_6 can be generated on the surface of WO_3 nanorods via *in-situ* crystal growth, so only a few heterojunctions are formed, making photocatalytic activity low. By increasing the concentration of Bi^{3+} ions, more heterojunctions are formed, thus resulting in the highest photocatalytic activity for the optimal S2 sample. However, upon further increasing the concentration of Bi^{3+} ions, WO_3 nanorods are completely covered by the dense Bi_2WO_6 nanosheets, as clearly observed in S3 sample (Fig. 2d), which makes the light irradiation on the junction interfaces and WO_3 nanorods decrease. This shielding effect of dense Bi_2WO_6 nanosheets coating on the WO_3 nanorods results in the low photocatalytic activity of S3 sample. Meanwhile, thick Bi_2WO_6 nanosheets reduce the BET surface area of S3, which leading to the decreased photocatalytic activity.

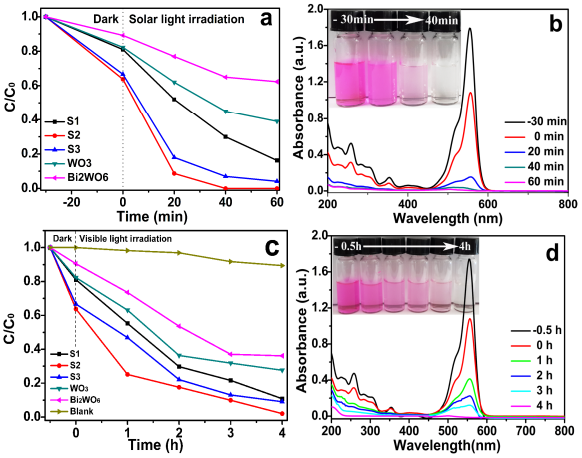

Fig. 8 (a, c) The degradation curves of RhB using different photocatalysts, (b, d) UV-Vis absorption spectra of RhB aqueous solutions using S2 as photocatalyst. Inset in b and d is photographs of RhB solutions at different irradiation time. (a,b) under solar light irradiation, (c,d) under visible light irradiation.

Fig. 8b displays the UV-Vis absorption spectra of RhB aqueous solutions using S2 as photocatalyst under solar light irradiation. It can be seen that all the absorption peaks of the RhB gradually decrease with prolonging irradiation time, and nearly disappear in 1 h. No new peaks appear during the whole photocatalytic process which indicates that the RhB melucules are successfully degraded. In addition, the removal of the ethyl groups and cleavage of the whole chromophore structure (cycloreversion) occur simultaneously for RhB molecules during the photocatalytic process, which can be proved by the photographs of RhB solutions (inset in Fig. 8b). From the mass spectra of RhB before and after being irradiated (Fig. S2), it can be seen that the peaks of molecular weight less than 331(m/z) do not appear in the mass spectrum (Fig. S2b) when RhB molecules are irradiated for 0.5 h in the presence of S2 photocatalyst. This implies that the whole chromophore structure for RhB molecule is degraded completely to CO_2 and H_2O.

The photocatalytic activity of the pure WO_3, Bi_2WO_6 and WO_3-Bi_2WO_6 heterojunctions was further evaluated by degradation of RhB dye under visible light irradiation ($\lambda > 400$ nm). As shown in Fig. 8c-d, S2 sample displays the highest photocatalytic activity among all the photocatlaysts for the degradation of RhB aqueous solution, and RhB can be completely decolored in 4 h under visible light irradiation (Fig. 8c). The degradation mechanism of RhB molecules is the same as that under solar light irradiation, which can be confirmed by the photograph (inset in Fig. 8d) and the UV-Vis absorbance spectra of RhB solution after photocatalytic reaction (Fig. 8d). Our results (degradation mechanism of RhB molecules) are different from the reports in refs 10, 22, 46. Compared to WO_3-Bi_2WO_6 composites with low photocatalytic activity in RhB degradation reported in ref 22, our sample displays higher photocatalytic activity for degradation of RhB under visible light.

In order to further evaluate the photocatalytic activity of the obtained samples, toxic organic phenol was chosen for photodegradation under solar light irradiation. It can be seen that sample S2 also has good photocatalytic performance for the degradation of phenol aqueous solution (Fig. S3), and can completely decompose phenol molecules within 100 min.

To investigate the stability of photocatalytic performance in solar light region, S2 sample was used to degrade RhB dye in five repeated cycles, and the results are shown in Fig. 9. It is noteworthy that S2 photocatalyst exhibits good photostability under solar light irradiation (Fig. 9a), and its photocatalytic efficiency only reduces 4% after 5 repeated cycles. From the XRD patterns (Fig. 9b) of the reused S2, it can be found that all the peaks are indexed to hexagonal phase WO_3 and orthorhombic Bi_2WO_6, and WO_3-Bi_2WO_6 heterojunctions still remain. These results demonstrate that S2 heterojunction has high stability in the process of cycling photocatalysis. From the SEM image, we also find that S2 still retained the original structure (Fig. 9c) after five repeated cycles.

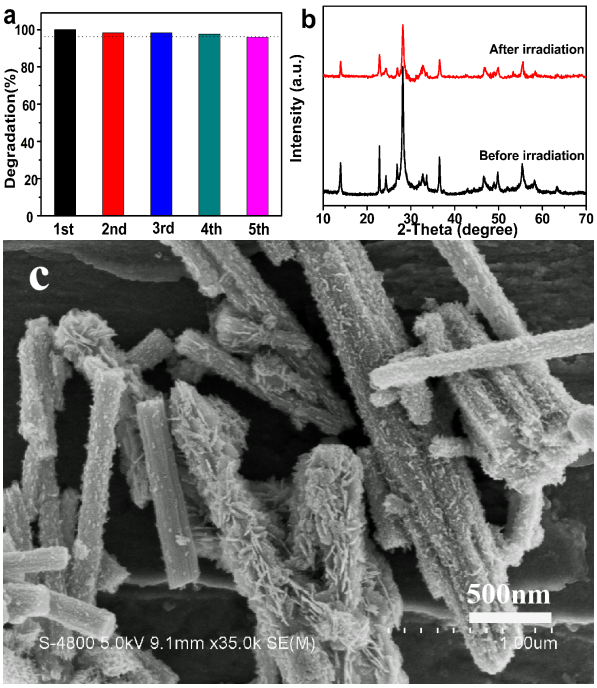

Fig. 9 (a) Cycling times of the photocatalytic degradation of RhB in the presence of S2 under solar light irradiation, (b) XRD pattern and (c) SEM image of the S2 after five repeated cycles.

In order to explore the photocatalytic mechanism of WO_3-Bi_2WO_6 heterojunctions in detail, the trapping experiments of active species during this photocatalytic process were carried out. Benzoquinone (BQ), tertbutyl alcohol (TBA), and EDTA-2Na were used as scavengers of superoxide radical ($\bullet O_2^-$), hydroxyl radical ($\bullet$OH) and h^+, respectively.[47–50] Fig. 10 shows the effect of different scavengers on the photodegradation rate over the S2 sample. it can be seen that the addition of EDTA-2Na and BQ causes significant deactivation of S2 photocatalyst, reducing the photocatalytic activity for degradation rate of RhB from 97% (30 min) to 19% and 23%, respectively. However, the photocatalytic performance of S2 only slightly decreases by the addition of TBA (Fig. 10). These results suggest that h^+ and $\bullet O_2^-$ radicals are the main active species rather than $\bullet$OH in the RhB photocatalytic process under solar light irradiation.

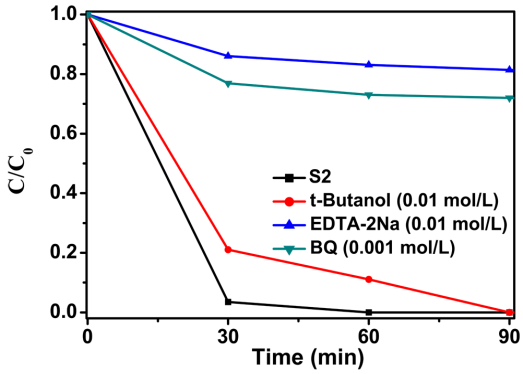

Fig. 10 Active species trapping experiments during the photocatalytic reaction for 90 min under solar light irradiation on S2 photocatalyst.

The relative positions of conduction band (CB) and valence band (VB) edges of WO_3, Bi_2WO_6 and S2 were measured. Fig. 11 shows valence band XPS (VB-XPS) of these three samples. In contrast to WO_3 (2.48 eV) and Bi_2WO_6 (2.28 eV), the VB edge of S2 is notably lowered down to 1.86 eV. The shift of VB maximum position for S2 can be attributable to the formation of WO_3-Bi_2WO_6 heterojunctions[10,50], as confirmed by XRD and HRTEM. According to the VB edges, combined with band gap of Bi_2WO_6 and WO_3, the CB edge potential of Bi_2WO_6 and WO_3 is −0.61 and −0.33 eV, respectively, calculated from the equation of $E_{CB} = E_{VB} - Eg$.

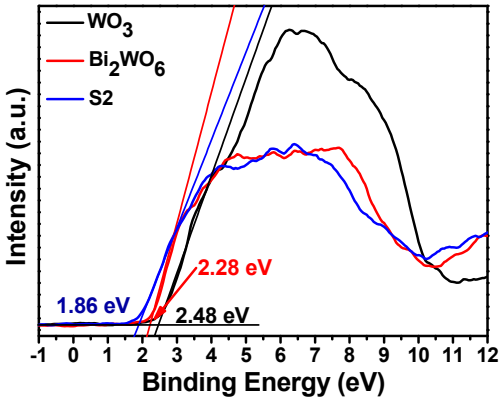

Fig. 11 VB-XPS spectra of WO_3, Bi_2WO_6 and S2 samples.

Based on results of the trapping experiments and the VB-XPS data, we readily illustrate the schematic diagram for photocatalytic reaction mechanism and charge transfer of the WO_3-Bi_2WO_6 heterostructures under solar light irradiation, as shown in Fig. 12. WO_3 and Bi_2WO_6 with narrow band gap can be excited by visible light and photogenerated electrons and holes are produced. When these two semiconductors are in contact to form WO_3-Bi_2WO_6 heterojunction, the excited electrons in the conduction band (CB) of Bi_2WO_6 can transfer to CB of WO_3 due to their different conduct band position, while the holes remain in the valence band of Bi_2WO_6. Meanwhile, the photogenerated holes on the valence band of WO_3 transfer to that of Bi_2WO_6 due to different valence band position, but the excited electrons stay in the conduct band of WO_3. Thus, the photogenerated electron-hole pairs in WO_3 and Bi_2WO_6 can be effectively separated and then the photocatalytic activity is significantly enhanced due to the formation of WO_3-Bi_2WO_6 heterojunctions.

From the Fig. 12, it can seen that the conduction band potential (-0.33 eV) of WO_3 is enough negative to E^0 (O_2/•O_2^-) (-0.046 eV vs NHE), the electrons left in the conduction band of WO_3 can reduce O_2 adsorbed on the surface of WO_3 nanorods to •O_2^- through one electron reducing reaction.[51] The oxidation potential of Bi_2WO_6 is 2.28 eV, which indicates that the photogenerated holes can not directly oxidize hydroxyl groups or water molecules adsorbed on the surface of Bi_2WO_6 to generate •OH radicals (2.7 V vs NHE). Hence, the h^+ and •O_2^- radicals rather than •OH are the main active species and react directly with RhB in the solution for efficient degradation.

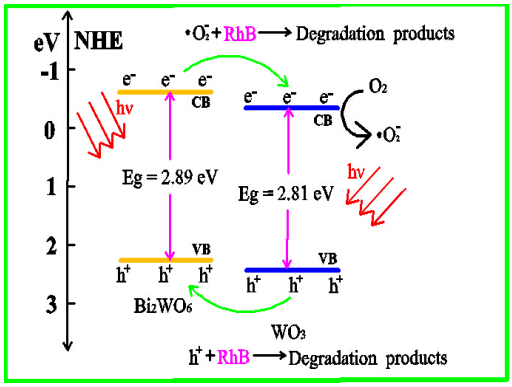

Fig. 12 Schematic diagram of photocatalytic mechanism of WO_3-Bi_2WO_6 heterojunction.

Conclusions

In summary, 1D WO_3-Bi_2WO_6 heterojunctions have been prepared for the first time via a facile hydrothermal method. Bi_2WO_6 nanosheets grow on the WO_3 nanorods. The obtained WO_3-Bi_2WO_6 heterojunctions exhibit higher photocatalytic activity than pure Bi_2WO_6 and WO_3 for the degradation of RhB under solar/visible light irradiation. RhB can be completely degraded in 60 min under solar light irradiation using WO_3-Bi_2WO_6 heterojunction as photocatalyst. This enhanced photocatalytic activity is due to the synergistic effects coming from the interfacial interactions between WO_3 and Bi_2WO_6, and efficient charge carrier transfer and separation. Moreover, 1D ordered nanostructures are favorable for highly efficient and directional transport and separation of electrons and holes. The WO_3-Bi_2WO_6 heterojunctions exhibit good stability after five repeated cycles. The h^+ and •O_2^- radicals are the main active species for photocatalytic degradation of RhB over WO_3-Bi_2WO_6. This work provides a facile and versatile strategy to fabricate other advanced materials with heterojunctions for potential photocatalytic and optoelectronic applications on a large scale.

Acknowledgements

This work is supported by the special funding support from the National Basic Research Program of China (2011CB933700, 2010CB934700) and the National Natural Science Foundation of China (21271165, 21101006).

Notes and references

‡ Additional figures and table are given in supporting information.

1 K. Sayama, K. Mukasa, R. Abe, Y. Abe and H. Arakawa, *Chem. Commun.*, 2001, **23**, 2416−2417.
2 R. Abe, T. Takata, H. Sugihara and K. Domen, *Chem. Commun.*, 2005, **37**, 3829−3831.

3 R. Abe, K. Sayama and H. Sugihara, *J. Phys. Chem. B,* 2005, **109**, 16052−16061.
4 K. Maeda, M. Higashi, D. Lu, R. Abe and K. Domen, *J. Am. Chem. Soc.,* 2010, **132**, 5858−5868.
5 Y. Sasaki, H. Kato and A. Kudo, *J. Am. Chem. Soc.,* 2013, **135**, 5441−5449.
6 K. Maeda, *ACS Catal.,* 2013, **3**, 1486−1503.
7 K. H. Reddy, S. Martha and K. M. Parida, *Inorg. Chem.,* 2013, **52**, 6390−6401.
8 Y. S. Xu, Z. J. Zhang and W. D. Zhang, *Dalton Trans.,* 2014, **43**, 3660-3668.
9 S. K. Pilli, R. Janarthanan, T. G. Deutsch, T. E. Furtak, L. D. Brown, J. A. Turnerd and A. M. Herring, *Phys. Chem. Chem. Phys.,* 2013, **15**, 14723−14728.
10 Y. Peng, M. Yan, Q. G. Chen, C. M. Fan, H. Y. Zhou and A. W. Xu, *J. Mater. Chem. A,* 2014, **2**, 8517−8524.
11 Y. F. Hou, S. J. Liu, J. H. Zhang, X. Cheng and Y. Wang, *Dalton Trans.,* 2014, **43**, 1025−1031.
12 X. Q. An, J. C. Yu, Y. Wang, Y. M. Hu, X. L. Yu and G. J. Zhang, *J. Mater. Chem.,* 2012, **22**, 8525–8531.
13 W. Wei, J. M. Xie, X. M. Lu, P. B. Osei, Z. X. Yan, S. C. Meng and H. L. Cui, *Monatsh. Chem.,* 2014, **145**, 47-59.
14 X. Lu, T. Zhai, X. Zhang, Y. Shen, L. Yuan, B. Hu, L. Gong, J. Chen, Y. Gao, J. Zhou, Y. Tong and Z. L. Wang, *Adv. Mater.,* 2012, **24**, 938–944.
15 A. Srinivasan and M. Miyauchi, *J. Phys. Chem. C,* 2012, **116**, 15421–15426.
16 X. Zhang, X. Lu, Y. Shen, J. Han, L. Yuan, L. Gong, Z. Xu, X. Bai, M. Wei, Y. Tong, Y. Gao, J. Chen, J. Zhou and Z. L. Wang, *Chem. Commun.,* 2011, **47**, 5804–5806.
17 M. A. Butler, R. D. Nasby and R. K. Quinn, *Solid State Commun.,* 1976, **19**, 1011–1014.
18 D. E. Scaife, *Sol. Energy,* 1980, **25**, 41–54.
19 L. H. Tian, L. Q. Ye, J. Y. Liu and L. Zan, *Catal. Commun.,* 2012, **17**, 99–103.
20 J. M. Berek and J. Sienko, *J. Solid State Chem.,* 1970, **2**, 109–133.
21 W. Smith, A. Wolcott, R. C. Fitzmorris, J. Z. Zhang and Y. P. Zhao, *J. Mater. Chem.,* 2011, **21**, 10792–10800.
22 M. S. Gui, W. D. Zhang, Y. Q. Chang and Y. X. Yu, *Chem. Eng. J.,* 2012, **197**, 283–288.
23 G. H. He, G. L. He, A. J. Li, X. Li, X. J. Wang, Y. P. Fang and Y. H. Xu, *J. Mol. Catal. A,* 2014, **385**, 106–111.
24 F. M. Wang, Y. J. Wang, X. Y. Zhan, M. Safdar, J. Gong and J. He, *CrystEngComm,* 2014, **16**, 1389–1394.
25 K. I. Liu, Y. C. Hsueh, H. S. Chen and T. P. Perng, *J. Mater. Chem. A,* 2014, **2**, 5387–5393.
26 C. W. Lai, S. Sreekantan, *Int. J. Hydrogen Energy,* 2013, **28**, 2156–2166.
27 L. Zhang, Y. G. Li, Q. H. Zhang and H. Z. Wang, *CrystEngComm,* 2013, **15**, 5986–5993.
28 A. Martínez-García, V. K. Vendra, S. Sunkara, P. Haldankar, J. Jasinski and M. K. Sunkara, *J. Mater. Chem. A,* 2013, **1**, 15235−15241.
29 C. Zhang and Y. F. Zhu, *Chem. Mater.,* 2005, **17**, 3537−3545.
30 F. Amano, A. Yamakata, K. Nogami, M. Osawa and B. Ohtani, *J. Am. Chem. Soc.,* 2008, **130**, 17650−17651.
31 G. S. Li, D. Q. Zhang, J. C. Yu and M. K. H. Leung, *Environ. Sci. Technol.,* 2010, **44**, 4276−4281.
32 J. Wang, E. Khoo, P. S. Lee and J. Ma, *J. Phys. Chem. C,* 2008, **112**, 14306–1431.
33 M. Penza, M. A. Tagliente, L. Mirenghi, C. Gerardi, C. Martucci and G. Cassano, *Sens. Actuators B,* 1998, **50**, 9–18.
34 B. Brunauer, L. S. Deming, W. S. Deming and E. J. Teller, *J. Am. Chem. Soc.,* 1940, **62**, 1723–1732.
35 T. Wang, X. Q. Yan, S. S. Zhao, B. Lin, C. Xue, G. D. Yang, S. J. Ding, B. L. Yang, C. S. Ma, G. Yang, G. R. A. Yang, *J. Mater. Chem. A,* 2014, **2**, 15611–15619.
36 X. Wang, J. C. Yu, C. Ho, Y. Hou and X. Fu, *Langmuir,* 2005, **21**, 2552−2559.
37 L. Z. Zhang and J. C. Yu, *Chem. Commun.,* 2003, **16**, 2078−2079.
38 C. S. Guo, M. Ge, L. Liu, G. D. Gao, Y. C. Feng and Y. Q. Wang, *Environ. Sci. Technol.,* 2010, **44**, 419−425.
39 Y. W. Mi, S. Y. Zeng, L. Li, Q. F. Zhang, S. N. Wang, C. H. Liu and D. Z. Sun, *Mater. Res. Bull.,* 2012, **47**, 2623−2630.
40 M. A. Butler, *J. Appl. Phys.,* 1977, **48**, 1914−1920.
41 Y. Y Guo, G. K. Zhang, H. H. Gan and Y. L. Zhang, *Dalton Trans.,* 2012, **41**, 12697−12703.
42 S. J. Hong, S. Lee, J. S. Jang and J. S. Lee, *Energy Environ. Sci.,* 2011, **4**, 1781–1787.
43 G. Leftheriotis, S. Papaefthimiou, P. Yianoulis, A. Siokou, *Thin solid films.,* 2001, **384**, 298−306.
44 J. Tian, Y. H. Sang, G. W. Yu, H. D. Jiang, X. N. Mu and H. Liu, *Adv. Mater.,* 2013, **25**, 5075–5080.
45 A. Rougier, F. Portemer, A. Quédé, M. El Marssi, *Appl. Surf. Sci.,* 1999, **153**, 1–9.
46 M. S. Gui, W. D. Zhang, Q. X. Su and C. H. Chen, *J. Solid State Chem.,* 2011, **184**, 1977−1982.
47 G. T. Li, K. H. Wong, X. W. Zhang, C. Hu, J. C. Yu, R. C. Y. Chan and P. K. Wong, *Chemosphere,* 2009, **76**, 1185–1191.
48 G. V. Buxton, C. L. Greenstock, W. P. Helman, A. B. Ross, *J. Phys. Chem. Ref. Data.,* 1988, **17**, 513–886.
49 X. K. Li, N. Kikugawa and J. H. Ye, *Adv. Mater.,* 2008, **20**, 3816–3819.
50 F. Dong, Y. J. Sun, M. Fu, Z. B. Wu and S. C. Lee, *J. Hazard. Mater.,* 2012, **219–220**, 26–34.
51 X. J. Wang, W. Y. Yang, F. T. Li, Y. B. Xue, R. H. Liu and Y. J. Hao, *Ind. Eng. Chem. Res.,* 2013, **52**, 17140–17150.

Graphic Abstract:

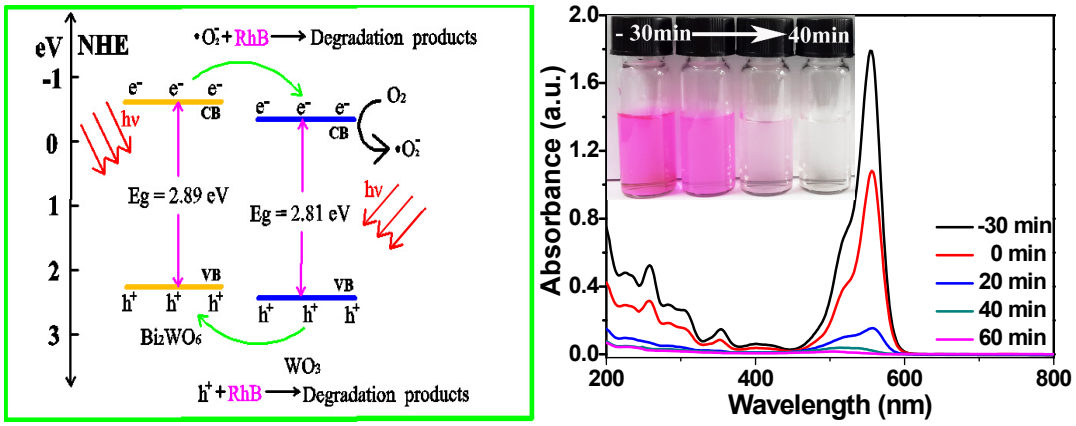

One-dimensional WO_3 -Bi_2WO_6 photocatalyst exhibits high photocatalytic activity for the degradation of Rhodamine B (RhB) under solar light irradiation, which is attributed to the effective separation of photogenerated electron-hole pairs by the stagger band potentials between WO_3 and Bi_2WO_6.